

Virtual corrections to $gg \rightarrow ZH$ in the high-energy and large- m_t limits

Joshua Davies^a, Go Mishima^b, Matthias Steinhauser^b

^a *Department of Physics and Astronomy, University of Sussex, Brighton BN1 9QH, UK*

^b *Department of Physics, Tohoku University, Sendai, 980-8578 Japan*

^c *Institut für Theoretische Teilchenphysik*

Karlsruhe Institute of Technology (KIT)

Wolfgang-Gaede Straße 1, 76128 Karlsruhe, Germany

Abstract

We compute the next-to-leading order virtual corrections to the partonic cross-section of the process $gg \rightarrow ZH$, in the high-energy and large- m_t limits. We use Padé approximants to increase the radius of convergence of the high-energy expansion in m_t^2/s , m_t^2/t and m_t^2/u and show that precise results can be obtained down to energies which are fairly close to the top quark pair threshold. We present results both for the form factors and the next-to-leading order virtual cross-section.

1 Introduction

At the CERN Large Hadron Collider (LHC), gluon fusion processes play an important role due to the large gluon luminosities at high collision energies. As a consequence one often observes that gluon fusion-induced processes provide a numerically large contribution to the theory predictions of production cross-sections. This is true even for processes for which the leading-order (LO) contribution consists of one-loop diagrams. A prime example of such a process is inclusive Higgs boson production, where the gluon-fusion channel is about an order of magnitude larger than all other contributions.

In this paper we consider the associated production of a Z and a Higgs boson, $pp \rightarrow ZH$, often called “Higgs Strahlung”. This process was of particular importance in the observation of the Higgs boson’s decay into bottom quarks at ATLAS [1] and CMS [2]. At LO it is mediated by a tree-level process in which a quark and anti-quark annihilate. For this channel, corrections up to next-to-next-to-next-to-leading ($N^3\text{LO}$) order are available [3] (see also Ref. [4] and references therein) and are included in the program `vh@nnlo` [5, 6]. Electroweak and QCD corrections are also included in the program `HAWK` [7].

Associated ZH production can also occur via the loop-induced gluon fusion process. Although formally of next-to-next-to-leading order (NNLO) with respect to $pp \rightarrow ZH$, it provides a sizeable contribution, in particular in the boosted Higgs boson regime in which the transverse momentum of the Higgs boson is large [8, 9]. Furthermore, the process $gg \rightarrow ZH$ provides sizeable contributions to the uncertainties of ZH production with a subsequent decay of the Higgs boson in a pair of bottom quarks, e.g., Ref. [10]. Being loop-induced, $gg \rightarrow ZH$ is sensitive to physics beyond the Standard Model. In Ref [11] it was suggested that the gluon-initiated component of $pp \rightarrow ZH$ can be extracted by comparing to WH production, which only has a Drell-Yan-like component. It is thus important to consider NLO QCD corrections to $gg \rightarrow ZH$, requiring the computation of two-loop box-type Feynman diagrams with two different final-state masses (m_Z and m_H) and the massive top quark propagating in the loops.

An exact LO (one-loop) calculation was performed in [12]. At NLO only approximations in the large m_t limit are known [13, 14]. In this work we consider the two-loop NLO virtual corrections in the high-energy limit, expanding the two-loop master integrals for $m_t^2 \ll s, t$, where s and t are the Mandelstam variables. Furthermore, we also provide analytic results for the form factors in the large- m_t limit.¹ A similar approach has been applied to the related process of Higgs boson pair production, $gg \rightarrow HH$, where a comparison to exact numerical calculations [15] could be performed and good agreement was found, even for relatively small values for the Higgs boson transverse momentum [16]. In Ref. [17] the high-energy expansion was successfully applied to the top quark contribution of the two-loop diagrams contributing to $gg \rightarrow ZZ$.

The remainder of the paper is organized as follows: In Section 2 we introduce our notation, and give our definitions for the form factors and the virtual finite cross-section.

¹In [14] only the squared amplitude has been computed.

In Section 3 we consider the quality of our approximations by comparing with the exact LO expressions. In Section 4, we briefly discuss the two-loop form factors in the large- m_t limit and in Section 5 we discuss the form factors in the high-energy limit, and investigate the behaviour of Padé approximants constructed using this expansion. In Section 6 we study the NLO virtual finite cross-section and apply our Padé scheme to extend the approximation to a larger kinematic region. Finally in Section 7 we conclude our findings. Auxiliary material can be found in the Appendix. In Appendix A we present analytic results for the one-particle reducible double-triangle contribution and in Appendix B we briefly discuss our treatment of γ_5 and the application of projectors to obtain the form factors. In Appendix C we present the relations between the form factors and helicity amplitudes for the process $gg \rightarrow ZH$. The expansions of the form factors are provided in an analytic, computer readable form in the ancillary files of this paper [18].

2 Notation and technicalities

We consider the amplitude for the process $g(p_1)g(p_2) \rightarrow Z(p_3)H(p_4)$ where all momenta are assumed to be incoming. This leads to the following definitions for the Mandelstam variables,

$$\begin{aligned} s &= (p_1 + p_2)^2, \\ t &= (p_1 + p_3)^2, \\ u &= (p_1 + p_4)^2, \end{aligned} \tag{1}$$

with

$$s + t + u = m_Z^2 + m_H^2. \tag{2}$$

Additionally, $p_1^2 = p_2^2 = 0$, $p_3^2 = m_Z^2$ and $(p_1 + p_2 + p_3)^2 = m_H^2$. We also introduce the transverse momentum (p_T) and the scattering angle (θ) of the final-state bosons, which are related to the Mandelstam variables as follows,

$$\begin{aligned} t &= -\frac{s}{2}(1 - \beta \cos \theta) + \frac{m_H^2 + m_Z^2}{2}, \\ u &= -\frac{s}{2}(1 + \beta \cos \theta) + \frac{m_H^2 + m_Z^2}{2}, \\ p_T^2 &= \frac{ut - m_H^2 m_Z^2}{s} = \frac{s}{4} \beta^2 \sin^2 \theta, \end{aligned} \tag{3}$$

where

$$\beta = \sqrt{1 - 2 \frac{m_Z^2 + m_H^2}{s} + \frac{(m_Z^2 - m_H^2)^2}{s^2}}. \tag{4}$$

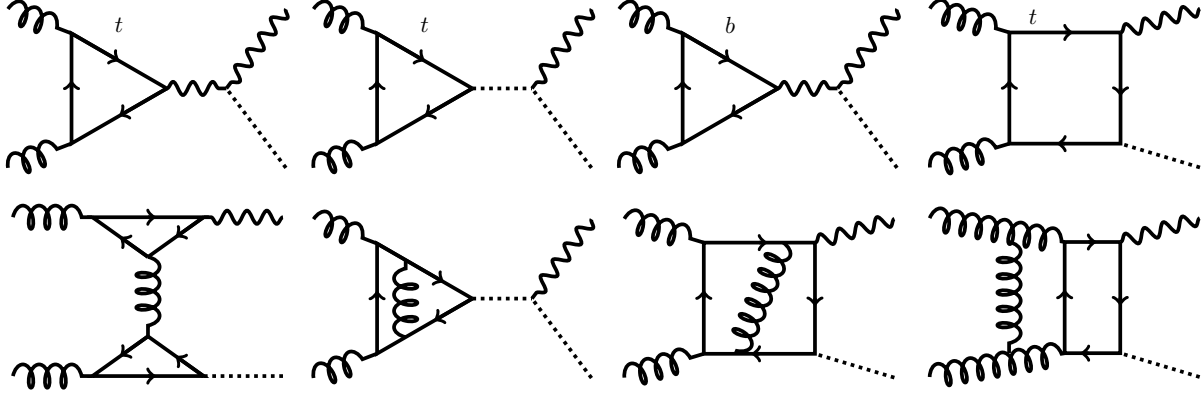


Figure 1: LO and NLO Feynman diagrams contributing to $gg \rightarrow ZH$. Curly, wavy and dashed lines represent gluons, Z bosons and scalar particles (Higgs or Goldstone bosons), respectively. Solid lines stand for top or bottom quarks. Note that the latter are only present in the triangle diagrams.

We denote the polarization vectors of the gluons and the Z boson by $\varepsilon_{\lambda_1,\mu}(p_1)$, $\varepsilon_{\lambda_2,\nu}(p_2)$ and $\varepsilon_{\lambda_3,\rho}(p_3)$, in terms of which the amplitude can be written as

$$\mathcal{M}_{\lambda_1,\lambda_2,\lambda_3} = A^{\mu\nu\rho} \varepsilon_{\lambda_1,\mu}(p_1) \varepsilon_{\lambda_2,\nu}(p_2) \varepsilon_{\lambda_3,\rho}(p_3). \quad (5)$$

Due to charge-conjugation invariance, the vector coupling of the Z boson to the quarks in the loop does not contribute. The axial-vector coupling is proportional to the third component of the isospin and thus mass-degenerate quark doublets also do not contribute. Since we consider the lightest five quarks to be massless, only contributions from the top-bottom doublet remain. Furthermore, each individual term of $A^{\mu\nu\rho}$ is proportional to the totally anti-symmetric ε tensor from the axial-vector coupling.

At LO and NLO both triangle- and box-type diagrams have to be considered. Examples of these diagram classes are shown in Fig. 1. In the box-type diagrams the Higgs boson couples directly to the quark loop, so diagrams involving the bottom quark are suppressed by their Yukawa coupling with respect to diagrams involving the top quark. This is not the case for the triangle-type diagrams; here contributions from both the top and bottom quark loops must be considered. At NLO there is also the contribution from the one-particle reducible double-triangle contribution, shown as first diagram in the second row of Fig. 1. Note that in the numerical results discussed in the main part of this paper these contributions are excluded, however, we present exact analytical results in Appendix A. The contribution from the reducible double-triangle diagrams to the (differential) partonic cross-section is implemented in the computer program which comes together with Ref. [14].

In total one can form 60 tensor structures from the indices μ, ν, ρ , the independent momenta p_1, p_2 and p_3 and an ε tensor. Details of the computation of these 60 structures and our treatment of γ_5 in $d = 4 - 2\epsilon$ dimensions are given in Appendix B. After

applying transversality conditions ($p_i \cdot \varepsilon_{\lambda_i}(p_i) = 0$), gauge invariance w.r.t. the gluons ($p_{1\mu} A^{\mu\nu\rho} = p_{2\nu} A^{\mu\nu\rho} = 0$) and Bose symmetry ($A^{\mu\nu\rho}(p_1, p_2, p_3) = A^{\nu\mu\rho}(p_2, p_1, p_3)$), 14 tensor structures remain which can be grouped such that one has to introduce 7 form factors. We follow the decomposition of Ref. [12] and write

$$\begin{aligned}
A_{ab}^{\mu\nu\rho}(p_1, p_2, p_3) &= i\delta_{ab} \frac{\sqrt{2}G_F M_Z}{s} \frac{\alpha_s(\mu)}{\pi} \tilde{A}^{\mu\nu\rho}(p_1, p_2, p_3), \\
\tilde{A}^{\mu\nu\rho}(p_1, p_2, p_3) &= \\
&\left\{ \left(\frac{s}{2} \varepsilon^{\mu\nu\rho\alpha} p_{2\alpha} - p_2^\mu \varepsilon^{\nu\rho\alpha\beta} p_{1\alpha} p_{2\beta} \right) F_1(t, u) - \left(\frac{s}{2} \varepsilon^{\mu\nu\rho\alpha} p_{1\alpha} - p_1^\nu \varepsilon^{\mu\rho\alpha\beta} p_{1\alpha} p_{2\beta} \right) F_1(u, t) \right. \\
&+ \left(p_3^\mu + \frac{m_Z^2 - t}{s} p_2^\mu \right) \varepsilon^{\nu\rho\alpha\beta} p_{2\alpha} \left[p_{1\beta} F_2(t, u) + p_{3\beta} F_3(t, u) \right] \\
&+ \left(p_3^\nu + \frac{m_Z^2 - u}{s} p_1^\nu \right) \varepsilon^{\mu\rho\alpha\beta} p_{1\alpha} \left[p_{2\beta} F_2(u, t) + p_{3\beta} F_3(u, t) \right] \\
&\left. + \left(\frac{s}{2} \varepsilon^{\mu\nu\rho\alpha} p_{3\alpha} - p_2^\mu \varepsilon^{\nu\rho\alpha\beta} p_{1\alpha} p_{3\beta} + p_1^\nu \varepsilon^{\mu\rho\alpha\beta} p_{2\alpha} p_{3\beta} + g^{\mu\nu} \varepsilon^{\rho\alpha\beta\gamma} p_{1\alpha} p_{2\beta} p_{3\gamma} \right) F_4(t, u) \right\}, \quad (6)
\end{aligned}$$

where a, b are colour indices. Note that while the decomposition is the same, the form factors in Ref. [12] have dimension $1/\text{GeV}^2$ whereas we pull out an overall factor of $1/s$ such that our form factors are dimensionless. Only F_1 receives contributions from the triangle-type diagrams discussed above. We represent the expansion coefficients of the form factors in the strong coupling constants with the following notation,

$$F = F^{(0)} + \frac{\alpha_s(\mu)}{\pi} F^{(1)} + \dots \quad (7)$$

At this point it is convenient to define new form factors which are linear combinations of those of Eq. (6),

$$\begin{aligned}
F_{12}(t, u) &= F_1(t, u) - \frac{t - m_Z^2}{s} F_2(t, u), \\
F_{12}(u, t) &= F_1(u, t) - \frac{u - m_Z^2}{s} F_2(u, t), \\
F_2^-(t, u) &= F_2(t, u) - F_2(u, t), \\
F_2^+(t, u) &= F_2(t, u) + F_2(u, t). \quad (8)
\end{aligned}$$

It is easy to see that $F_2^+(t, u)$ drops out in the squared amplitude and thus does not contribute to physical quantities. It is furthermore convenient to introduce

$$\begin{aligned}
F_{12}^-(t, u) &= F_{12}(t, u) - F_{12}(u, t), \\
F_{12}^+(t, u) &= F_{12}(t, u) + F_{12}(u, t), \\
F_3^-(t, u) &= F_3(t, u) - F_3(u, t),
\end{aligned}$$

$$F_3^+(t, u) = F_3(t, u) + F_3(u, t), \quad (9)$$

leaving six physically relevant functions:

$$F_{12}^+(t, u), \quad F_{12}^-(t, u), \quad F_2^-(t, u), \quad F_3^+(t, u), \quad F_3^-(t, u), \quad F_4(t, u), \quad (10)$$

where only $F_{12}^+(t, u)$ has contributions from triangle-type diagrams. $F_k^-(t, u)$ (with $k = 12, 2, 3$) and $F_4(t, u)$ are anti-symmetric w.r.t. the exchange of the arguments t, u , and $F_k^+(t, u)$ (with $k = 12, 3$) are symmetric. At leading order $F_3^-(t, u) = 0$, however it has non-zero contributions starting at NLO.

For the computation of the one- and two-loop Feynman diagrams (some examples are shown in Fig. 1) in the high-energy limit, we proceed as follows: After producing the amplitude we perform a Taylor expansion in the Z and Higgs boson masses (since $m_Z^2, m_H^2 \ll m_t^2$), leaving one- and two-loop integrals which depend only on s , t and m_t . Using integration-by-parts reduction techniques with the programs **FIRE 6** [19] and **LiteRed** [20], these integrals can be reduced to the same basis of 161 two-loop master integrals as in Refs. [21, 22], in which they were computed as an expansion in the high-energy limit to order m_t^{32} . Inserting these expansions into the amplitude yields its high-energy approximation. We use **FORM 4.2** [23] for most stages of the computation. The calculation is performed in the covariant R_ξ gauge and we allow for a general electroweak gauge parameter ξ_Z which appears in the propagators of the Z boson and Goldstone boson χ . Thus only the triangle-type diagrams depend on ξ_Z , and this dependence cancels upon summing the Z and χ contributions.

We also investigate the large- m_t limit of the form factors. This expansion is straightforward and proceeds in analogy to [17, 22]. The programs **q2e** and **exp** [24, 25] are used to produce an asymptotic expansion for $m_t \gg q_1, q_2, q_3$, again performed using **FORM**, yielding products of massive vacuum integrals and massless three-point integrals. Results for the $gg \rightarrow ZH$ amplitude, expanded to order $1/m_t^8$, have been previously published in [14]; here we provide one additional term in this expansion, to order $1/m_t^{10}$, and provide results at the level of the form factors.

The renormalization of the ultra-violet (UV) divergences proceeds in a similar way as for the processes $gg \rightarrow HH$ [22] and $gg \rightarrow ZZ$ [17]. In particular, we work in the six-flavour theory and renormalize the top quark mass on shell and the strong coupling α_s in the $\overline{\text{MS}}$ scheme. In addition, our treatment of γ_5 (see Appendix B for more details) requires that we apply additional finite renormalization to the axial and pseudo-scalar currents [26],

$$\begin{aligned} Z_{5A} &= 1 - \frac{\alpha_s}{\pi} C_F + \mathcal{O}(\epsilon), \\ Z_{5P} &= 1 - 2 \frac{\alpha_s}{\pi} C_F + \mathcal{O}(\epsilon). \end{aligned}$$

The subtraction of the infra-red poles proceeds according to Ref. [27], using the conventions of Refs. [17, 22]. The subtraction has the form [27]

$$F^{(1)} = F^{(1),\text{IR}} - K_g^{(1)} F^{(0)} = \tilde{F}^{(1)} + \beta_0 \log \left(\frac{\mu^2}{-s - i\delta} \right) F^{(0)}, \quad (11)$$

with $\beta_0 = 11C_A/12 - Tn_f/3$ and $F^{(1),\text{IR}}$ is UV renormalized but still infra-red (IR) divergent. $F^{(1)}$ is finite. An explicit expression for K_g is given in Eq. (2.3) of Ref. [22]. After the second equality sign in Eq. (11) we make the μ dependence explicit. Note that below we only need $\tilde{F}^{(1)}$ to construct the NLO cross-section.

In analogy to the process $gg \rightarrow HH$ [28] we define the NLO virtual finite cross-section for $gg \rightarrow ZH$ as

$$\begin{aligned} \tilde{\mathcal{V}}_{\text{fin}} = & \frac{G_F^2 m_Z^2}{16s^2} \left(\frac{\alpha_s}{\pi} \right)^2 \sum_{\lambda_1, \lambda_2, \lambda_3} \left\{ \left[\tilde{A}_{\text{sub}}^{\mu\nu\rho} \tilde{A}_{\text{sub}}^{\star, \mu'\nu'\rho'} \right]^{(1)} + \frac{C_A}{2} \left(\pi^2 - \log^2 \frac{\mu^2}{s} \right) \left[\tilde{A}_{\text{sub}}^{\mu\nu\rho} \tilde{A}_{\text{sub}}^{\star, \mu'\nu'\rho'} \right]^{(0)} \right\} \\ & \times \varepsilon_{\lambda_1, \mu}(p_1) \varepsilon_{\lambda_1, \mu'}^*(p_1) \varepsilon_{\lambda_2, \nu}(p_2) \varepsilon_{\lambda_2, \nu'}^*(p_2) \varepsilon_{\lambda_3, \rho}(p_3) \varepsilon_{\lambda_3, \rho'}^*(p_3), \end{aligned} \quad (12)$$

where the form factors entering the amplitude $\tilde{A}_{\text{sub}}^{\mu\nu\rho}$ are the IR-subtracted finite form factors $\tilde{F}^{(1)}$ of Eq. (11). The superscripts “(0)” and “(1)” after the square brackets in Eq. (12) indicate that we take the coefficients of $(\alpha_s/\pi)^0$ and $(\alpha_s/\pi)^1$, respectively, of the squared amplitude, in accordance with Eq. (7). For the discussion in Section 6 it is convenient to introduce the α_s -independent quantity

$$\mathcal{V}_{\text{fin}} = \frac{\tilde{\mathcal{V}}_{\text{fin}}}{\alpha_s^2}. \quad (13)$$

3 Comparison at leading order

In this section we compare our high-energy expansion with the exact LO result. We implement this by using **FeynArts** [29] to generate the amplitude and **FormCalc** [30] to compute it, performing a Passarino-Veltman reduction to three- and four-point one-loop scalar integrals. Schouten identities allow us to write the result in terms of the tensor structures and form factors of Eqs. (6) and (8). We use **Package-X** [31] to evaluate the Passarino-Veltman functions with high precision and to produce an analytic expansion in the limit of a large top quark mass. We have verified that our implementation of the exact LO result reproduces the cross-sections provided in the literature [13, 14, 32]. Additionally we have compared the large- m_t expansion derived from this result with a direct expansion of the amplitude as described above.

In Fig. 2 we show the squared amplitude at LO, as a function of \sqrt{s} , for a fixed scattering angle $\theta = \pi/2$. The solid black lines correspond to the exact result. The coloured lines correspond to different expansion depths in m_Z and m_H , as detailed in the plot legend. All of the latter include high-energy expansion terms up to m_t^{32} . The red curve demonstrates that after including quadratic terms both in m_H and m_Z , the deviation from the exact result is below 1% (for $\sqrt{s} \gtrsim 1000$ GeV). The m_H^2 corrections appear to be more important than the m_Z^2 corrections. The inclusion of the quartic terms (shown as green and pink curves, best visible in Fig. 2(c)) improves the accuracy of the expansion, leading to an almost negligible deviation from the exact expression. These terms are much

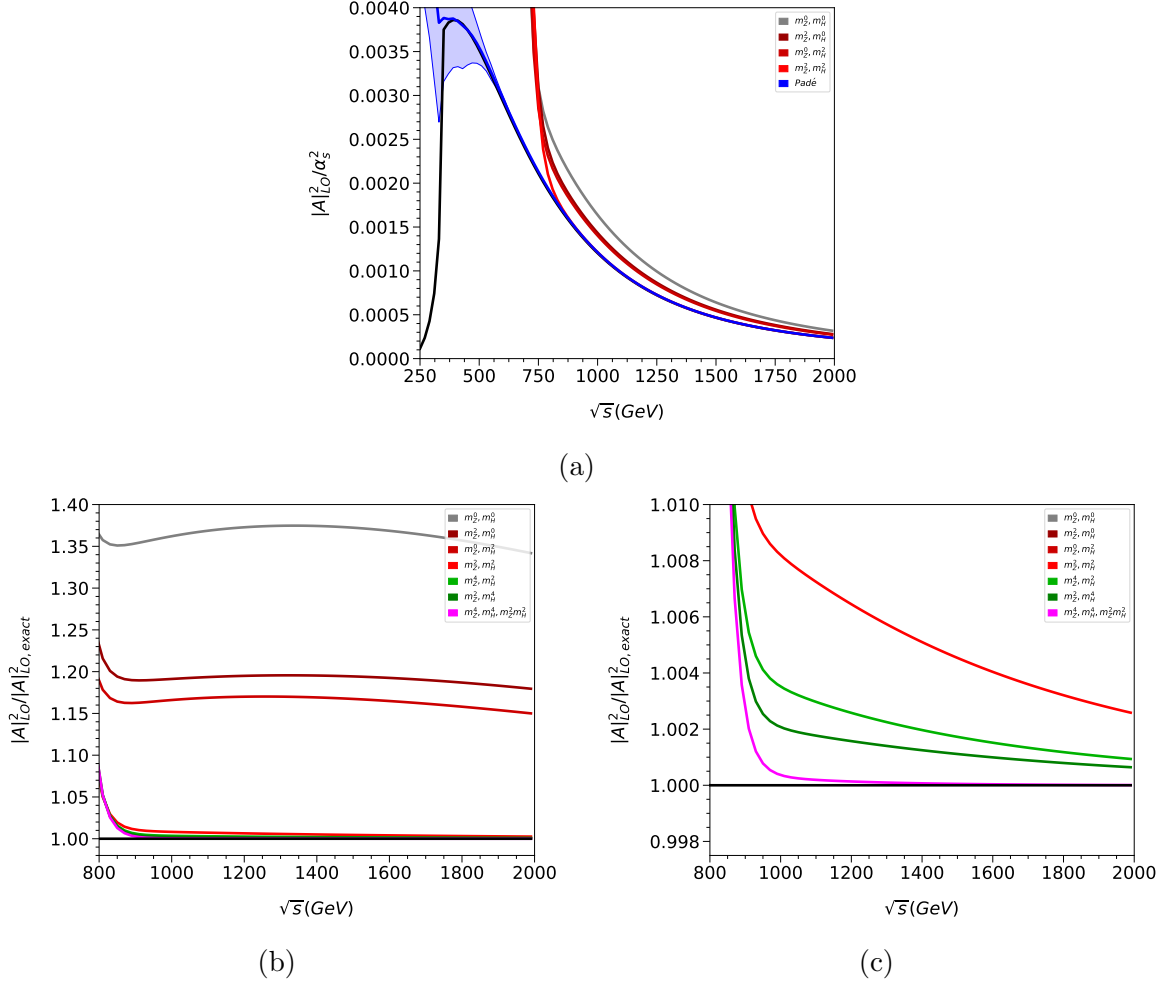


Figure 2: (a) LO squared amplitude and (b) ratio of expansions to the exact result. Plot (c) is a zoomed-in version of (b). Note that for better readability in (a) no quartic corrections are shown; the black curve in (a) refers to the exact result and the blue curve (and associated uncertainty band) is the result obtained from Padé approximation.

harder to compute, however, so in the NLO results we will restrict the approximation to the quadratic corrections only. The solid blue curve and associated uncertainty band in Fig. 2(a) shows the result of a procedure to improve the expansions based on Padé approximants, which is discussed in more detail in Section 5. Here it is based on the expansion to quadratic order in m_H and m_Z , confirming that our computation of the NLO amplitude only to this order is sufficient.

In Fig. 2 and in the following sections, we use the following parameter values:

$$m_Z = 91.1876 \text{ GeV}, m_t = 172.9 \text{ GeV}, m_H = 125.1 \text{ GeV}, G_F = 1.16638 \times 10^{-5} \text{ GeV}^{-2}. \quad (14)$$

4 NLO form factors: large- m_t limit

In this section we discuss the large- m_t expansion of the form factors at NLO. While the expansion of \tilde{F}_{12}^+ starts at m_t^0 , we find that the other form factors of Eq. (10) exhibit some cancellation in the leading contributions. In particular, \tilde{F}_{12}^- , \tilde{F}_2^- , \tilde{F}_3^+ and \tilde{F}_4 start only at $1/m_t^4$, and \tilde{F}_3^- starts at $1/m_t^6$.

We now present the leading terms of the large- m_t expansion to establish our notation. For brevity, we restrict ourselves to \tilde{F}_{12}^+ . Expressions for the expansion of all form factors to $1/m_t^{10}$ are provided in the ancillary files of this paper [18]. Our result reads

$$\begin{aligned} \tilde{F}_{12}^{+, (1)} = & -2C_A + \frac{s}{m_t^2} \left(\frac{11C_A}{72} - \frac{C_F}{4} \right) + \frac{1}{m_t^4} \left(C_F s \left[\frac{222m_H^2 + 162m_Z^2 - 263s}{2160} \right] \right. \\ & + C_A \left(\frac{1}{129600} \left[-75 \left\{ m_H^4 + m_Z^4 - \frac{6}{5} m_H^2 m_Z^2 \right\} + 4011m_H^2 s + 6713m_Z^2 s \right. \right. \\ & \left. \left. - 2646s^2 + 60 \{ m_H^2 + m_Z^2 - s - t \} t \right] - s \log \left(\frac{-s}{m_t^2} \right) \left[\frac{9m_H^2 + 26m_Z^2 - 9s}{2160} \right] \right) , \end{aligned} \quad (15)$$

where $C_A = 3$ and $C_F = 4/3$ are the quadratic Casimir invariants of $SU(3)$.

We have verified that after constructing $\tilde{\mathcal{V}}_{\text{fin}}$ in Eq. (12) we find agreement with the results of Ref. [14] up to order $1/m_t^8$.

5 NLO form factors: high-energy limit

We now turn to the high-energy expansion of the NLO form factors. The analytic expressions are large, so we refrain from showing them here but we provide analytic expressions for all form factors in the ancillary files of this paper [18]. For illustration we discuss in the following the results for \tilde{F}_3^+ .

In Fig. 3(a) we plot \tilde{F}_3^+ as a function of \sqrt{s} . We can see that the high-energy expansions of both the real (blue solid lines) and imaginary parts (green dashed lines) converge well for $\sqrt{s} \gtrsim 800$ GeV, which is in analogy to $gg \rightarrow HH$ [22] and $gg \rightarrow ZZ$ [17]. Note that the lighter-coloured curves include fewer m_t expansion terms; the darkest lines show the expansion up to m_t^{32} .

As in previous publications on $gg \rightarrow HH$ and $gg \rightarrow ZZ$, we make use of Padé approximants to improve the description of the high-energy expansion. The methodology used follows that of Section 4 of Ref. [17] and so is not described in detail, but is only summarized briefly here. The expansion is used to produce 28 different Padé approximants, which are combined to produce a central value and error estimate for the approximation. In Fig. 3(a) the Padé results are shown as red bands. The width of the bands denote the uncertainty estimates. For regions in which the high-energy expansion converges, the

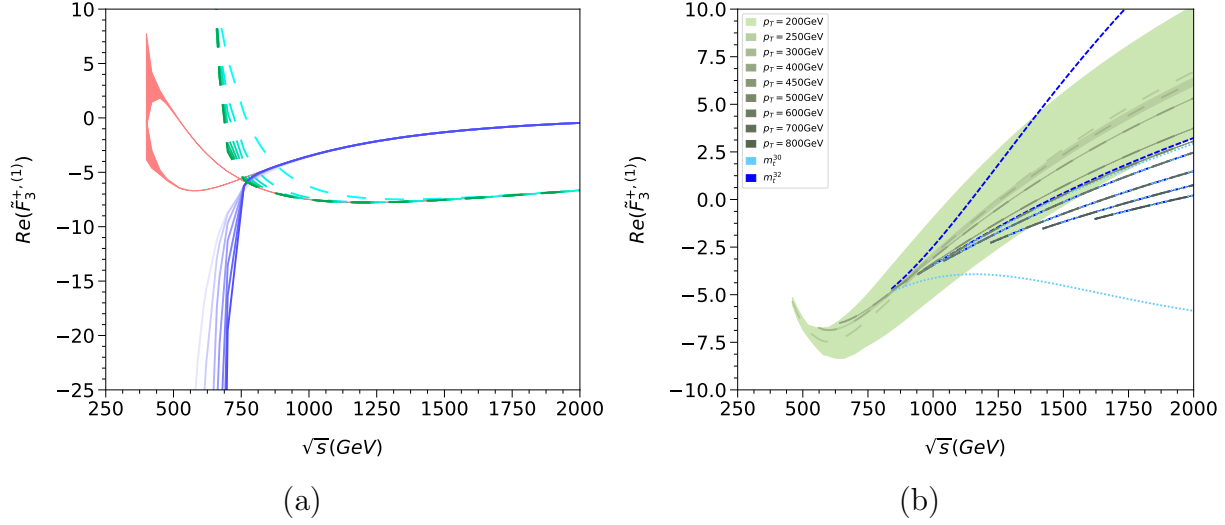


Figure 3: Results for \tilde{F}_3^+ as a function of \sqrt{s} for fixed $\theta = \pi/2$ (a) and for fixed p_T (b). In (a) dashed and solid lines correspond to the imaginary and real parts, respectively. The red curves in (a) represent the Padé results. In (b) only the real part is shown, and the Padé results are shown as green dashed lines. The high-energy expansions up to order m_t^{30} and m_t^{32} are shown in blue. The widely-separated pair of curves correspond to $p_T = 400$ GeV.

Padé-based approximation reproduces the expansion. However, it also produces reliable results for smaller values of \sqrt{s} , as can be expected from the comparison with the LO result shown in Fig. 2(a).

In Fig. 3(b) we show \tilde{F}_3^+ for the fixed values of $p_T = 200, \dots, 800$ GeV. The blue (dashed and dotted) curves correspond to the high-energy expansions and the green (dashed) curves to the Padé results. For all Padé curves we also show the corresponding uncertainty band, which for $p_T = 200$ GeV is relatively large but for $p_T = 250$ GeV the uncertainty band is already quite small; it is completely negligible for higher values of p_T . Note that the high-energy expansions are only shown for $p_T \geq 400$ GeV; for lower p_T values the curves lie far outside of the plot range. For $p_T \gtrsim 450$ GeV the expansions converge and are very close to the Padé results. For $p_T = 400$ GeV, while the expansions initially agree with each other and the Padé close to $\sqrt{s} = 800$ GeV, they diverge for larger values of \sqrt{s} . We recall here that the high-energy expansion is an expansion in m_t^2/s , m_t^2/t and m_t^2/u . For a fixed value of p_T , increasing \sqrt{s} can lead to values of t or u which are not large enough for convergence.

In Section 6 we will apply the Padé procedure to the virtual finite cross-section, in order to compare our results with a state-of-the-art numerical evaluation at NLO [33].

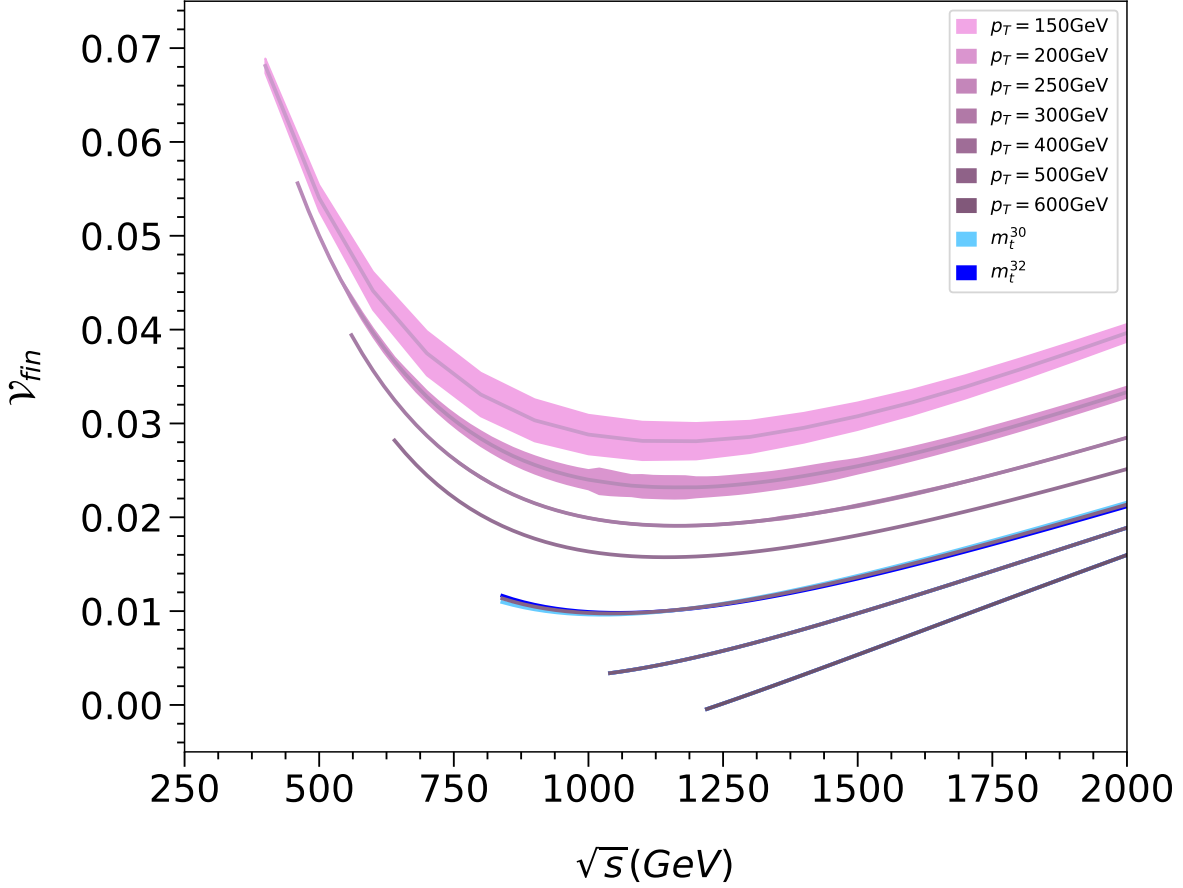


Figure 4: \mathcal{V}_{fin} as a function of \sqrt{s} for eight values of p_T , at the scale $\mu^2 = s$. The uncertainty estimate of the Padé procedure is displayed as light-coloured bands. For $p_T \geq 350$ GeV, we also show two high-energy expansion curves including terms up to order m_t^{30} and m_t^{32} .

6 NLO virtual finite cross-section

Our starting point is $\tilde{\mathcal{V}}_{\text{fin}}$ in Eq. (12). For the LO form factors we use the exact results and for the two-loop form factors we use the high-energy expansion. This allows us to write \mathcal{V}_{fin} in Eq. (13) as an expansion in m_t up to order m_t^{32} .² At this point we can apply the Padé approximation procedure as described in Section 5. In Fig. 4 we show \mathcal{V}_{fin} for several fixed values of p_T as a function of \sqrt{s} . For $p_T = 400$ GeV and larger we also show two high-energy expansion curves, which include terms up to m_t^{30} and m_t^{32} . These curves agree well with each other and with the Padé approximation which they produce. For lower values of p_T , these curves do not agree with each other, and are not visible within

²Note the double-triangle contribution, which is known analytically (see Appendix A and Ref. [14]), is not included in our numerical results for \mathcal{V}_{fin} .

the plot range.

For $p_T = 150$ GeV Padé procedure produces stable results with an uncertainty of about 10%. For $p_T = 200$ GeV the uncertainties are notably smaller and for higher p_T values they are negligible. We advocate to use results based on our approach for $p_T \gtrsim 200$ GeV. For $p_T \approx 150$ GeV the Padé approach provides important results for cross-checks. For lower values of p_T other methods have to be used for the calculation of $gg \rightarrow ZH$, see Ref. [33].

We have compared our results with those of Ref. [33], which are obtained numerically, but without making any expansions. In the high-energy region, for 104 kinematic points with $p_T \geq 200$ GeV we agree to within 2-3%, and for 42 points with $150 \leq p_T < 200$ GeV we agree to within 10% and our values are consistent to within the uncertainty of the Padé procedure. We also construct \mathcal{V}_{fin} using the large- m_t expanded NLO form factors of Section 4 and find that for 120 points with $\sqrt{s} \leq 284$ GeV, we agree to within 1%. For larger values of \sqrt{s} , as expected, the large- m_t expansion starts to diverge significantly from the numerical results as one approaches the top quark threshold at $\sqrt{s} \approx 346$ GeV.

7 Conclusions

In this paper we consider two-loop NLO corrections to the Higgs Strahlung process $gg \rightarrow ZH$. The corresponding Feynman integrals involve five dimensionful parameters (s , t , m_t , m_Z and m_H) which makes an analytic calculation impossible with the current state-of-the-art techniques. Numerical computations are also very challenging, however they have recently been achieved in Ref. [33]. In Section 6 we have discussed the cross-check of our results against these.

In our approach we use the hierarchy between the top quark, Higgs and Z boson masses and perform an expansion for $m_t^2 \gg m_Z^2, m_H^2$, effectively eliminating the dependence on m_Z and m_H from the integrals. We show at one-loop order that the expansion converges quickly, which allows us to truncate the expansion at NLO after the quadratic terms. As far as the remaining scales are concerned, we concentrate on the high-energy region where $s, t \gg m_t^2$. We expand our master integrals in this limit such that we obtain results for the form factors including expansion terms up to m_t^{32} . This allows us to construct, for each phase-space point (e.g., a particular pair of \sqrt{s} , p_T values) a set of Padé approximants, which considerably extend the region of convergence of our expansion. Our approach provides both central values and uncertainty estimates.

We provide results for all form factors involved in the $gg \rightarrow ZH$ amplitude, both at one- and two-loop order. Furthermore, we provide relations between the form factors and helicity amplitudes in Appendix C. The main emphasis of the paper is the IR subtracted virtual corrections to the partonic cross-section, which can be combined with other (e.g. Drell-Yan-like) corrections to $gg \rightarrow ZH$. Our method provides precise results for $p_T \gtrsim 200$ GeV with almost negligible uncertainties. For lower values of p_T our uncer-

tainties increase, in particular for smaller values of \sqrt{s} . The analytic results for the form factors obtained in this paper can be obtained in electronic form from Ref. [18].

Acknowledgements. We thank the authors of Ref. [33] for making their results available for comparison, prior to publication. The work of J.D. was in part supported by the Science and Technology Research Council (STFC) under the Consolidated Grant ST/T00102X/1. The work of G.M. was in part supported by JSPS KAKENHI (No. JP20J00328). This research was supported by the Deutsche Forschungsgemeinschaft (DFG, German Research Foundation) under grant 396021762 — TRR 257 “Particle Physics Phenomenology after the Higgs Discovery”.

A Double-triangle contribution

In this appendix we present results for the one-particle reducible double-triangle contribution, as shown in the first diagram in the second row of Fig. 1. We have computed the six form factors in Eq. (10). The results can be expressed in terms of the functions (see also Ref. [34] where the corresponding contributions for $gg \rightarrow HH$ were computed)

$$\begin{aligned} B_0(x, 0, 0) &= 2 - \log \frac{-x}{\mu^2}, \\ B_0(x, m^2, m^2) &= 2 + \beta_x \log \frac{\beta_x - 1}{\beta_x + 1} - \log \frac{m^2}{\mu^2}, \\ C_0(x, y, 0, m^2, m^2, m^2) &= \frac{1}{2(x - y)} \left(\log^2 \frac{\beta_x + 1}{\beta_x - 1} - \log^2 \frac{\beta_y + 1}{\beta_y - 1} \right), \end{aligned} \quad (16)$$

with $\beta_x = \sqrt{1 - 4m^2/x}$ and $\beta_y = \sqrt{1 - 4m^2/y}$. Our explicit calculation shows that $F_3^+(t, u) = F_3^-(t, u) = F_4(t, u) = 0$. We furthermore find that $F_{12}(t, u)$ is equal to $F_2(t, u)$ with

$$\begin{aligned} F_2(t, u) &= \frac{8m_t^2 m_Z^2 s}{(m_H^2 - u)^2 (m_Z^2 - u)^2} \left\{ 2u [B_0(m_H^2, m_t^2, m_t^2) - B_0(u, m_t^2, m_t^2)] \right. \\ &\quad \left. + (m_H^2 - u) [(-m_H^2 + 4m_t^2 + u) C_0(u, m_H^2, 0, m_t^2, m_t^2, m_t^2) + 2] \right\} \\ &\quad \times \left[B_0(u, m_t^2, m_t^2) - B_0(m_Z^2, m_t^2, m_t^2) + B_0(m_Z^2, 0, 0) - B_0(u, 0, 0) \right. \\ &\quad \left. + 2m_t^2 \frac{u - m_Z^2}{m_Z^2} C_0(u, m_Z^2, 0, m_t^2, m_t^2, m_t^2) \right], \end{aligned} \quad (17)$$

which can be used to construct $F_{12}^+(t, u)$, $F_{12}^-(t, u)$ and $F_2^-(t, u)$ (cf. Section 2). We note that it is straightforward to expand the results in Eq. (17) in the large- and small- m_t limit.

The contribution of the double-triangle diagrams to the squared matrix element have been computed in Ref. [14] and implemented in the corresponding computer program, see Appendix of Ref. [14].

B Projectors and γ_5

Each LO and NLO diagram contributing to the $gg \rightarrow ZH$ amplitude contains a quark with either an axial-vector coupling to a Z boson, or a pseudo-scalar coupling to a Goldstone boson. The γ_5 matrix present in these couplings is not defined in the $d = 4 - 2\epsilon$ space-time dimensions of dimensional regularization. The couplings are re-written in terms of anti-symmetric tensors, according to [26], as

$$\begin{aligned}\gamma^\mu \gamma^5 &= \frac{i}{12} \varepsilon^{\mu\nu\rho\sigma} (\gamma_\nu \gamma_\rho \gamma_\sigma - \gamma_\sigma \gamma_\rho \gamma_\nu) , \\ \gamma^5 &= \frac{i}{96} \varepsilon^{\mu\nu\rho\sigma} (\gamma_\mu \gamma_\nu \gamma_\rho \gamma_\sigma + \gamma_\sigma \gamma_\rho \gamma_\nu \gamma_\mu - \gamma_\nu \gamma_\rho \gamma_\sigma \gamma_\mu - \gamma_\mu \gamma_\sigma \gamma_\rho \gamma_\nu) ,\end{aligned}\quad (18)$$

which allow one to compute the loop integrals in two ways. The first is to ensure the ε tensors are not contracted until one can safely work in four dimensions, by solving tensor loop integrals, performing UV renormalization and IR subtraction (as detailed in Eq. (11)) and then finally contracting with the ε tensors.

An alternative approach, which avoids the need to compute tensor integrals, is to project the amplitude onto the 60 possible rank-three Lorentz structures which can be formed from the three independent momenta and the ε tensor. Since each term of the projectors onto these structures contains an ε tensor, the result of their contraction with the r.h.s. of Eq. (18) can be treated correctly in d dimensions. The 60 projectors act on the amplitude as

$$P_i^{\mu_1\mu_2\mu_3} A_{\mu_1\mu_2\mu_3} = F_i \quad (19)$$

to produce 60 form factors F_i , which can be reduced to a minimal set (see the discussion around Eq. (6)). Each projector $P_i^{\mu_1\mu_2\mu_3}$ can be written generically as

$$C_{i,1} \varepsilon^{\mu_1\mu_2\mu_3\nu_1} q_{1\nu_1} + C_{i,2} \varepsilon^{\mu_1\mu_2\mu_3\nu_1} q_{2\nu_1} + \dots + C_{i,60} g^{\mu_1\mu_2} \varepsilon^{\mu_3\nu_1\nu_2\nu_3} q_{1\nu_1} q_{2\nu_2} q_{3\nu_3} , \quad (20)$$

and we contract this general form with our amplitude. In the final result, we specify each of the 60 sets of coefficients $\{C_{i,j}\}$ in order to obtain the 60 form factors F_i .

C Helicity amplitudes

In this appendix we describe how one can obtain the helicity amplitudes for the process $gg \rightarrow ZH$ from the tensor decomposition which we have introduced in Section 2. In

analogy to Eq. (5) we introduce

$$\tilde{\mathcal{M}}_{\lambda_1, \lambda_2, \lambda_3} = \tilde{A}^{\mu\nu\rho} \varepsilon_{\lambda_1, \mu}(p_1) \varepsilon_{\lambda_2, \nu}(p_2) \varepsilon_{\lambda_3, \rho}(p_3). \quad (21)$$

We furthermore specify the (contravariant) external momenta and polarization vectors as follows:

$$\begin{aligned} p_1 &= \frac{\sqrt{s}}{2} \begin{pmatrix} 1 \\ 0 \\ 0 \\ 1 \end{pmatrix}, \quad p_2 = \frac{\sqrt{s}}{2} \begin{pmatrix} 1 \\ 0 \\ 0 \\ -1 \end{pmatrix}, \quad p_3 = \frac{\sqrt{s}}{2} \begin{pmatrix} -y_1 \\ 0 \\ -y_2 \sin \theta \\ y_2 \cos \theta \end{pmatrix}, \quad p_4 = \frac{\sqrt{s}}{2} \begin{pmatrix} -2 + y_1 \\ 0 \\ y_2 \sin \theta \\ -y_2 \cos \theta \end{pmatrix}, \\ \varepsilon_+(p_1) &= [\varepsilon_-(p_1)]^* = \frac{1}{\sqrt{2}} \begin{pmatrix} 0 \\ i \\ 1 \\ 0 \end{pmatrix}, \quad \varepsilon_+(p_2) = [\varepsilon_-(p_2)]^* = \frac{1}{\sqrt{2}} \begin{pmatrix} 0 \\ -i \\ 1 \\ 0 \end{pmatrix}, \\ \varepsilon_+(p_3) &= [\varepsilon_-(p_3)]^* = \frac{1}{\sqrt{2}} \begin{pmatrix} 0 \\ i \\ \cos \theta \\ \sin \theta \end{pmatrix}, \quad \varepsilon_0(p_3) = \frac{\sqrt{s}}{2m_Z} \begin{pmatrix} y_2 \\ 0 \\ y_1 \sin \theta \\ -y_1 \cos \theta \end{pmatrix}, \\ y_1 &= 1 + \frac{m_Z^2 - m_H^2}{s}, \quad y_2 = \beta = \sqrt{1 - 2 \frac{m_Z^2 + m_H^2}{s} + \frac{(m_Z^2 - m_H^2)^2}{s^2}}, \end{aligned} \quad (22)$$

where ε_0 denotes the longitudinal components of polarization vectors. Recall that all external momenta are defined as incoming, see Eq. (1). We have chosen the convention for the polarisation vector of p_2 , following Ref. [35], such that $\varepsilon_+(p_2) \rightarrow \varepsilon_-(p_1)$ in the center-of-momentum frame. Furthermore, the polarization vectors satisfy

$$\begin{aligned} \sum_{\lambda_1} \varepsilon_{\lambda_1, \mu}(p_1) \varepsilon_{\lambda_1, \mu'}^*(p_1) &= -g_{\mu\mu'} + \frac{p_{1,\mu} p_{2,\mu'} + p_{2,\mu} p_{1,\mu'}}{p_1 \cdot p_2}, \\ \sum_{\lambda_2} \varepsilon_{\lambda_2, \nu}(p_2) \varepsilon_{\lambda_2, \nu'}^*(p_2) &= -g_{\nu\nu'} + \frac{p_{2,\nu} p_{1,\nu'} + p_{1,\nu} p_{2,\nu'}}{p_1 \cdot p_2}, \\ \sum_{\lambda_3} \varepsilon_{\lambda_3, \rho}(p_3) \varepsilon_{\lambda_3, \rho'}^*(p_3) &= -g_{\rho\rho'} + \frac{p_{3,\rho} p_{3,\rho'}}{m_Z^2}, \end{aligned} \quad (23)$$

which means that we have fixed the gauge for the external gauge bosons. With the above choice, some of the tensor structures in $A_{ab}^{\mu\nu\rho}(p_1, p_2, p_3)$, which are proportional to either p_1^ν or p_2^μ , are irrelevant because

$$\varepsilon_{\lambda_1}(p_1) \cdot p_2 = \varepsilon_{\lambda_2}(p_2) \cdot p_1 = 0. \quad (24)$$

This reduces the number of Lorentz structures in Eq. (6) from 14 to 8. We note that, as we will see in Eq. (28), the dependence on F_2^+ drops out in the helicity amplitude.

In total there are $2 \times 2 \times 3 = 12$ helicity amplitudes. However, due to various symmetries, only 4 of them are independent. With explicit calculation we find

$$\begin{aligned}\tilde{\mathcal{M}}_{-\lambda_1, -\lambda_2, -\lambda_3} &= -\tilde{\mathcal{M}}_{\lambda_1, \lambda_2, \lambda_3}, \\ \tilde{\mathcal{M}}_{++-} &= -\tilde{\mathcal{M}}_{+++} \Big|_{\theta \rightarrow \theta + \pi, y_2 \rightarrow -y_2}, \\ \tilde{\mathcal{M}}_{+--} &= -\tilde{\mathcal{M}}_{-+-} \Big|_{\theta \rightarrow \theta + \pi, y_2 \rightarrow -y_2},\end{aligned}\tag{25}$$

yielding the 4 independent helicity amplitudes. Note that the Mandelstam variables are invariant under the simultaneous replacements $\theta \rightarrow \theta + \pi, y_2 \rightarrow -y_2$ and thus the form factors do not change.

For the evaluation of the ε tensor, we use the convention that

$$\varepsilon^{0123} = +1,\tag{26}$$

and so some of the relevant contractions are as follows:

$$\begin{aligned}\varepsilon^{\mu\rho\alpha\beta}\varepsilon_{\mu+}(p_1)\varepsilon_{\rho+}(p_3)p_{1\alpha}p_{2\beta} &= -i\frac{s}{4}(1 - \cos\theta), \\ \varepsilon^{\mu\rho\alpha\beta}\varepsilon_{\mu+}(p_1)\varepsilon_{\rho+}(p_3)p_{1\alpha}p_{3\beta} &= i\frac{s}{8}(1 - \cos\theta)(y_1 - y_2), \\ \varepsilon^{\rho\alpha\beta\gamma}\varepsilon_{\rho+}(p_3)p_{1\alpha}p_{2\beta}p_{3\gamma} &= -i\frac{s\sqrt{s}}{4\sqrt{2}}y_2\sin\theta, \\ \varepsilon^{\mu\rho\alpha\beta}\varepsilon_{\mu+}(p_1)\varepsilon_{\rho 0}(p_3)p_{1\alpha}p_{2\beta} &= i\frac{s\sqrt{s}}{4\sqrt{2}m_Z}y_1\sin\theta, \\ \varepsilon^{\mu\rho\alpha\beta}\varepsilon_{\mu+}(p_1)\varepsilon_{\rho 0}(p_3)p_{1\alpha}p_{3\beta} &= -i\frac{m_Z\sqrt{s}}{2\sqrt{2}}\sin\theta, \\ \varepsilon^{\mu\nu\rho\alpha}\varepsilon_{\mu+}(p_1)\varepsilon_{\nu+}(p_2)\varepsilon_{\rho+}(p_3)p_{1\alpha} &= i\frac{\sqrt{s}}{2\sqrt{2}}\sin\theta, \\ \varepsilon^{\mu\nu\rho\alpha}\varepsilon_{\mu+}(p_1)\varepsilon_{\nu+}(p_2)\varepsilon_{\rho 0}(p_3)p_{1\alpha} &= -i\frac{s}{4m_Z}(y_1\cos\theta + y_2).\end{aligned}\tag{27}$$

In terms of the form factors, the 4 independent helicity amplitudes read

$$\begin{aligned}\tilde{\mathcal{M}}_{+-0} &= -i\frac{s}{16m_Z}y_2\sin^2\theta(sy_1F_2^- - 2m_Z^2F_3^-) \\ \tilde{\mathcal{M}}_{+--} &= i\frac{s\sqrt{s}}{16\sqrt{2}}y_2\sin\theta(1 - \cos\theta)(2F_2^- - y_1F_3^- - y_2F_3^+) \\ \tilde{\mathcal{M}}_{+++} &= i\frac{s\sqrt{s}}{16\sqrt{2}}\sin\theta[4F_{12}^- - (y_1 - y_2)(2F_2^- + 4F_4 + y_2F_3^- + y_2\cos\theta F_3^+)] \\ \tilde{\mathcal{M}}_{++0} &= -i\frac{s}{8m_Z}[(sy_1F_{12}^- - 2m_Z^2F_2^- - 4m_Z^2F_4)\cos\theta - sy_2F_{12}^+ + m_Z^2y_2\sin^2\theta F_3^+],\end{aligned}\tag{28}$$

where we have omitted the arguments of the form factors, $F(t, u)$.

These helicity amplitudes have some general properties which are valid at any loop order. It is useful to introduce the partial wave decomposition of the amplitude [35]

$$\mathcal{M}_{\lambda_a, \lambda_b, \lambda_c} = \frac{1}{4\pi} \sum_J (2J+1) \langle \lambda_c | S^J | \lambda_a \lambda_b \rangle d_{\lambda_a - \lambda_b, \lambda_c}^J(\theta), \quad (29)$$

where λ_a, λ_b ($= \pm 1$ in this case) are the helicities of initial state particles and λ_c ($= \pm 1, 0$) is the helicity of the Z boson. J is the total angular momentum of the system, S^J is the J -component of the S-matrix, and $d_{M, M'}^J(\theta)$ is the Wigner small- d function (see, e.g. [36]). In the case of \mathcal{M}_{++0} ,

$$d_{\lambda_a - \lambda_b, \lambda_c}^J(\theta) = d_{0,0}^J(\theta) = P_J(\cos \theta), \quad (30)$$

where $P_J(x)$ are the Legendre polynomials, which are even functions for even J , and odd functions for odd J . Taking into account that F_{12}^-, F_2^-, F_3^- and F_4 are anti-symmetric in $t \leftrightarrow u$ exchange and thus odd functions in $\cos \theta$, whereas F_{12}^+ and F_3^+ are symmetric in $t \leftrightarrow u$ exchange and thus even functions in $\cos \theta$, we find that \mathcal{M}_{++0} is an even function of $\cos \theta$. Using Eq. (29) and the property of the Legendre polynomials mentioned above, we conclude that only J -even components contribute to \mathcal{M}_{++0} and thus this amplitude is a J -even channel. In a similar discussion, it is also straightforward to show that \mathcal{M}_{+-0} , expanded in terms of $d_{2,0}^J(\theta) = P_2^J(\cos \theta)$ where P_2^J is the associated Legendre polynomial, is a J -odd channel, and that \mathcal{M}_{+++} , expanded in terms of $d_{0,1}^J(\theta) = P_1^J(\cos \theta)$, is a J -even channel. On the other hand, \mathcal{M}_{+-+} does not have such a feature. In total, the squared amplitude should be symmetric in $t \leftrightarrow u$ exchange due to the fact that the two initial state gluons are indistinguishable, and this symmetry is made apparent when summing all of the squared helicity amplitudes.

The contribution from the triangle diagrams is present only in \mathcal{M}_{++0} via F_{12}^+ , and this can be understood in the following way. Due to the Landau-Yang theorem, the on-shell mode of the mediating Z -boson is forbidden; only the off-shell mode and the Goldstone boson propagate. Since the off-shell mode and the Goldstone boson behave as scalars under rotation, they do not appear in \mathcal{M}_{+-0} (J -odd) or \mathcal{M}_{+-+} (J -indefinite). Furthermore, using the transversal condition of the Z -boson, $\varepsilon_{\pm}(p_3) \cdot p_3 = 0$ one can also derive that $\varepsilon_{\pm}(p_3) \cdot p_4 = 0$ and thus the transverse components of the final state Z -boson do not couple to the scalar-scalar-vector interaction (see, e.g., the explicit form of the Feynman rule for the Goldstone-Higgs- Z boson vertex). Because of this property, the contribution from triangle diagrams is absent in \mathcal{M}_{+++} ; only \mathcal{M}_{++0} (and \mathcal{M}_{-0} , due to Eq. (25)) contains such contributions.

References

- [1] M. Aaboud *et al.* [ATLAS], Phys. Lett. B **786** (2018), 59-86 [arXiv:1808.08238 [hep-ex]].

- [2] A. M. Sirunyan *et al.* [CMS], Phys. Rev. Lett. **121** (2018) no.12, 121801 doi:10.1103/PhysRevLett.121.121801 [arXiv:1808.08242 [hep-ex]].
- [3] M. C. Kumar, M. K. Mandal and V. Ravindran, JHEP **03** (2015), 037 [arXiv:1412.3357 [hep-ph]].
- [4] G. Heinrich, [arXiv:2009.00516 [hep-ph]].
- [5] O. Brein, R. V. Harlander and T. J. E. Zirke, Comput. Phys. Commun. **184** (2013), 998-1003 [arXiv:1210.5347 [hep-ph]].
- [6] R. V. Harlander, J. Klappert, S. Liebler and L. Simon, JHEP **05** (2018), 089 [arXiv:1802.04817 [hep-ph]].
- [7] A. Denner, S. Dittmaier, S. Kallweit and A. Mück, Comput. Phys. Commun. **195** (2015), 161-171 [arXiv:1412.5390 [hep-ph]].
- [8] C. Englert, M. McCullough and M. Spannowsky, Phys. Rev. D **89** (2014) no.1, 013013 [arXiv:1310.4828 [hep-ph]].
- [9] R. V. Harlander, S. Liebler and T. Zirke, JHEP **02** (2014), 023 [arXiv:1307.8122 [hep-ph]].
- [10] G. Aad *et al.* [ATLAS], [arXiv:2007.02873 [hep-ex]].
- [11] R. V. Harlander, J. Klappert, C. Pandini and A. Papaefstathiou, Eur. Phys. J. C **78** (2018) no.9, 760 [arXiv:1804.02299 [hep-ph]].
- [12] B. A. Kniehl, Phys. Rev. D **42** (1990) 2253.
- [13] L. Altenkamp, S. Dittmaier, R. V. Harlander, H. Rzehak and T. J. Zirke, JHEP **02** (2013), 078 doi:10.1007/JHEP02(2013)078 [arXiv:1211.5015 [hep-ph]].
- [14] A. Hasselhuhn, T. Luthe and M. Steinhauser, JHEP **1701** (2017) 073 [arXiv:1611.05881 [hep-ph]].
- [15] S. Borowka, N. Greiner, G. Heinrich, S. P. Jones, M. Kerner, J. Schlenk and T. Zirke, JHEP **1610** (2016) 107 [arXiv:1608.04798 [hep-ph]].
- [16] J. Davies, G. Heinrich, S. P. Jones, M. Kerner, G. Mishima, M. Steinhauser and D. Wellmann, JHEP **11** (2019), 024 [arXiv:1907.06408 [hep-ph]].
- [17] J. Davies, G. Mishima, M. Steinhauser and D. Wellmann, JHEP **04** (2020), 024 [arXiv:2002.05558 [hep-ph]].
- [18] <https://www.ttp.kit.edu/preprints/2020/ttp20-041/>.
- [19] A. V. Smirnov and F. S. Chuharev, [arXiv:1901.07808 [hep-ph]].

- [20] R. N. Lee, J. Phys. Conf. Ser. **523** (2014), 012059 [arXiv:1310.1145 [hep-ph]].
- [21] J. Davies, G. Mishima, M. Steinhauser and D. Wellmann, JHEP **03** (2018), 048 [arXiv:1801.09696 [hep-ph]].
- [22] J. Davies, G. Mishima, M. Steinhauser and D. Wellmann, JHEP **01** (2019), 176 [arXiv:1811.05489 [hep-ph]].
- [23] B. Ruijl, T. Ueda and J. Vermaseren, [arXiv:1707.06453 [hep-ph]].
- [24] R. Harlander, T. Seidensticker and M. Steinhauser, Phys. Lett. B **426** (1998) 125 [hep-ph/9712228].
- [25] T. Seidensticker, hep-ph/9905298.
- [26] S. Larin, Phys. Lett. B **303** (1993), 113-118 [arXiv:hep-ph/9302240 [hep-ph]].
- [27] S. Catani, Phys. Lett. B **427** (1998) 161 [hep-ph/9802439].
- [28] G. Heinrich, S. P. Jones, M. Kerner, G. Luisoni and E. Vryonidou, JHEP **08** (2017), 088 [arXiv:1703.09252 [hep-ph]].
- [29] T. Hahn, Comput. Phys. Commun. **140** (2001), 418-431 [arXiv:hep-ph/0012260 [hep-ph]].
- [30] T. Hahn and M. Perez-Victoria, Comput. Phys. Commun. **118** (1999), 153-165 [arXiv:hep-ph/9807565 [hep-ph]].
- [31] H. H. Patel, Comput. Phys. Commun. **218** (2017), 66-70 [arXiv:1612.00009 [hep-ph]].
- [32] O. Brein, M. Ciccolini, S. Dittmaier, A. Djouadi, R. Harlander and M. Kramer, [arXiv:hep-ph/0402003 [hep-ph]].
- [33] L. Chen, G. Heinrich, S.P. Jones M. Kerner, J. Klappert and J. Schlenk, ZU-TH 45/20, CERN-TH-2020-199, IPPP/20/57, P3H-20-076, KA-TP-21-2020, TTK-20-42, PSI-PR-20-21.
- [34] G. Degrandi, P. P. Giardino and R. Gröber, Eur. Phys. J. C **76** (2016) no.7, 411 doi:10.1140/epjc/s10052-016-4256-9 [arXiv:1603.00385 [hep-ph]].
- [35] M. Jacob and G. C. Wick, Annals Phys. **7** (1959), 404-428
- [36] J. J. Sakurai and J. Napolitano, “Modern Quantum Mechanics,” Cambridge University Press.